Broadband and wide-angle blazed acoustic gratings using multiple coupled Helmholtz resonators

2017 Appl. Phys. Express 10 097201

(http://iopscience.iop.org/1882-0786/10/9/097201)

Applied Physics Express **10**, 097201 (2017)
https://doi.org/**10.7567/APEX.10.097201**

Broadband and wide-angle blazed acoustic gratings using multiple coupled Helmholtz resonators

Yongkang Dong[1], Gaokun Yu[1]*, Xinlong Wang[2], Xiaoyu Niu[1], Kai Wu[1], and Ning Wang[1]

[1]*Department of Marine Technology, Ocean University of China, Qingdao 266100, China*
[2]*Key Laboratory of Modern Acoustics and Institute of Acoustics, Nanjing University, Nanjing 210093, China*

*E-mail: gkyu@ouc.edu.cn

Received July 19, 2017; accepted August 14, 2017; published online September 1, 2017

By combining Helmholtz resonances and Bragg scatterings, perfect acoustic blazing, a type of acoustic Wood's anomaly, is achieved at the Bragg blazing points and non-Bragg blazing points. Owing to couplings among these blazing points, we experimentally observe a broadband and wide-angle acoustic negative reflection by an acoustic grating based on multiple coupled Helmholtz resonators per cell with a subwavelength thickness of 25.7 mm, where the frequency range is 3430 to 5145 Hz. © 2017 The Japan Society of Applied Physics

Blazed gratings can reflect most of the incident power into one diffraction order at a specified wavelength. When the specular reflection disappears completely and the total incident power is diffracted into a single diffraction order, such as the −1st order, perfect blazing is achieved. This phenomenon is a type of Wood's anomaly; such anomalies were first observed by Wood[1)] in experiments on reflection gratings. Wood's anomalies can usually be categorized into two distinct types: one is the Rayleigh wavelength type, which results from the emergence of a new spectral order at the grazing angle,[2)] and the other type is related to resonances supported by the optical grating (free complex resonances).[3)] Perfect blazing by a rectangular groove grating was observed at the Bragg blazing points along the Bragg line[4)] or at the non-Bragg blazing points,[5)] which occur in pairs on opposite sides of the Bragg line. It is noted that the combination of local resonances[4–7)] (or hybridized surface resonant states[3,8)]) and the Bragg scattering effect leads to perfect blazing for various gratings. This concept has been extended to acoustics, for example, back reflection at a specified wavelength,[9)] the observation of acoustical "transparency",[10)] and the blazed phononic crystal grating.[11,12)]

To broaden the bandwidth and reduce the grating thickness, multiple coupled Helmholtz resonators[13)] are introduced in this paper to design a blazed acoustic grating with multiple Bragg blazing points and non-Bragg blazing points located in the region where the specular and (−1st or 1st) orders are the only propagating diffraction orders. At the blazing points, perfect acoustic blazing, that is, the Wood's anomaly induced by local resonances supported by the acoustic grating, is achieved. Owing to couplings among the blazing resonances (at the blazing points), our designed blazed acoustic grating exhibits a wide frequency-angle range of negative acoustic reflection.

We study broadband and wide-angle negative reflection from a blazed acoustic grating placed in a two-dimensional waveguide, as shown in Fig. 1(a). The design of an acoustic grating based on six coupled Helmholtz resonators per cell is shown in Fig. 1(b). Using a procedure similar to that in Ref. 14, in the following, we derive the reflection coefficient of the acoustic grating and discuss the formation of perfect acoustic blazing. We assume a unit incident sound pressure, $p_i = \exp(jk\sin\theta_i x + jk\cos\theta_i z)$, where θ_i is defined as the angle of incidence with respect to the normal in Fig. 1(b). According to Floquet's theory, the sound fields on the side ($z < 0$) can be expanded in series, $p_r = \sum_m r_m e^{jk\beta_m x + k\alpha_m z}$, where r_m is the reflection coefficient of the mth diffraction

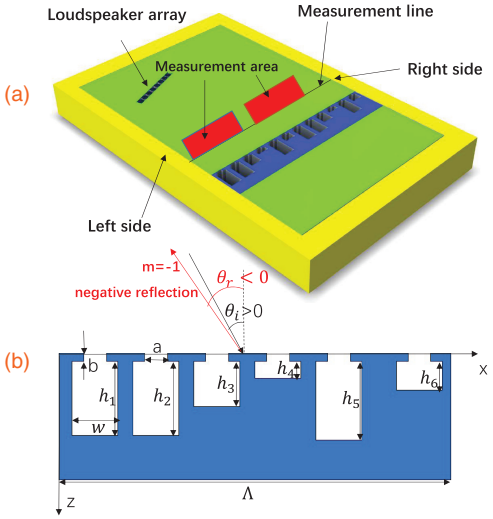

Fig. 1. (a) Experimental scheme of acoustic negative reflection. (b) Corresponding dimensions of the acoustic grating: the lattice constant $\Lambda = 80$ mm, the thickness of the grating is 25.7 mm, the size of the throat $a = 5$ mm, the length of the throat $b = 2$ mm, the width of the cavity $w = 10$ mm, the heights of the six cavities $h_1 = 0.2197\Lambda$, $h_2 = 0.2190\Lambda$, $h_3 = 0.1346\Lambda$, $h_4 = 0.0508\Lambda$, $h_5 = 0.2339\Lambda$, $h_6 = 0.0854\Lambda$.

order with the horizontal wavenumber $k\beta_m = k\sin\theta_i + 2\pi m/\Lambda \equiv k\sin\theta_{mr}$ and the vertical wavenumber $jk\alpha_m = k\sqrt{1-\beta_m^2}$, for $m = 0, \pm1, \pm2, \ldots$. By introducing the volume velocity $U_a(n)$ at position x_n (the inlet of the nth Helmholtz resonator in the unit cell), we obtain, from the continuity of sound pressure and normal velocity at the boundary $z = 0$,

$$Z_a(n)U_a(n) + \sum_{n'} Z_{nn'}U_a(n') = 2e^{jkx_n\sin\theta_i}\Phi_0^*(\theta_i), \qquad (1)$$

where $Z_a(n)$ is the acoustic impedance of a Helmholtz resonator at position x_n without coupling, and $Z_{nn'} = \sum_m (j\alpha_m)^{-1}R_\Sigma e^{jk\beta_m(x_n - x_{n'})}|\Phi_m(\theta_i)|^2$ with $\Phi_m(\theta_i) = (a/2)\int_{-a/2}^{a/2} e^{-jk\beta_m x}\,dx$ represents the couplings among multiple Helmholtz resonators. The relationship between the reflection coefficient r_m and $U_a(n)$ is

$$r_m = \delta_{0m} - (j\alpha_m)^{-1}\Phi_m(\theta_i)R_\Sigma \sum_{n'} U_a(n')e^{-jk\beta_m x_{n'}}, \qquad (2)$$

where δ_{0m} is the Kronecker delta, $R_\Sigma \equiv \rho_0 c_0/\Lambda$, and $\rho_0 c_0$ is the characteristic acoustical impedance of air. Perfect blazing is achieved by setting the specular reflection coefficient $r_0 = 0$, and the total incident power is diffracted into the −1st (or 1st) order when the specular and −1st (or 1st) orders

are the only propagating diffraction orders. Considering this constraint, Eq. (2) can be rewritten as $\Phi_0^*(\theta_i) = (j\alpha_0)^{-1}|\Phi_0(\theta_i)|^2 R_\Sigma \sum_{n'} U_a(n') e^{-jk\sin\theta_i x_{n'}}$. Substituting this formula into Eq. (1), we obtain

$$Z_a(n)U_a(n) + \sum_{n'} X_{nn'} U_a(n') = 0 \tag{3}$$

with $X_{nn'} = \sum_m (1 - 2\delta_{0m})(j\alpha_m)^{-1} R_\Sigma e^{jk\beta_m(x_n - x_{n'})}|\Phi_m(\theta_i)|^2$. Because Eq. (3) has nonzero solutions, we can obtain the position of the blazing point at a specified frequency and incident angle.

For an acoustic grating based on a single Helmholtz resonator per cell, Eq. (3) is simplified as

$$Z_a(1) + \sum \frac{R_\Sigma}{j\alpha_m}|\Phi_m(\theta_i)|^2 - \frac{2R_\Sigma|\Phi_0(\theta_i)|^2}{\cos\theta_i} = 0 \tag{4}$$

For a positive incident angle, $\theta_i > 0$, we obtain from Eq. (4) the Bragg condition, $k\sin\theta_i = \pi/\Lambda$, and an equation determined by the Helmholtz resonance and the evanescent waves supported by the acoustic grating,

$$\mathrm{Im}\left(Z_a(1) + \sum_{m\neq 0,\neq -1} \frac{R_\Sigma}{j\alpha_m}|\Phi_m(\theta_i)|^2\right) = 0.$$

The above two relations determine the angle and frequency at which perfect blazing is achieved. Because the blazing point is located on the Bragg line determined by the Bragg condition, it is called the Bragg blazing point. Note that for an acoustic grating based on a single Helmholtz resonator per cell, no non-Bragg blazing point exists, which can be easily verified from Eq. (4).

For acoustic gratings based on multiple coupled Helmholtz resonators per cell, calculation of Eq. (3) indicates that perfect blazing can occur at frequencies away from the resonance frequencies of the Helmholtz resonators owing to the coupling term in Eq. (3). However, the blazing points can always be observed along the Bragg line, and thus the corresponding blazing points are also called Bragg blazing points. To understand the coupling effect, an acoustic grating based on two coupled Helmholtz resonators per cell is chosen to analyze the condition of perfect blazing, mainly for its simplicity. When the incident angle θ_i is positive and the interval between the two coupled Helmholtz resonators is $\Lambda/2$, we obtain, from the condition of a nonzero solution of Eq. (3),

$$\begin{vmatrix} \tilde{Z}_a(1) + \tilde{Z}_{-1} - \tilde{Z}_0 & \tilde{Z}_{12} - \tilde{Z}_{-1} - \tilde{Z}_0 \\ \tilde{Z}_{12} - \tilde{Z}_{-1} - \tilde{Z}_0 & \tilde{Z}_a(2) + \tilde{Z}_{-1} - \tilde{Z}_0 \end{vmatrix} = 0 \tag{5}$$

where $\tilde{Z}_0 = R_\Sigma/(\cos\theta_i)|\Phi_0(\theta_i)|^2$, $\tilde{Z}_{-1} = R_\Sigma/(j\alpha_{-1})|\Phi_{-1}(\theta_i)|^2$, $\tilde{Z}_a(1) = Z_a(1) + \sum_{m\neq 0,-1} R_\Sigma/(j\alpha_m)|\Phi_m(\theta_i)|^2$, and $\tilde{Z}_a(2) = Z_a(2) + \sum_{m\neq 0,-1} R_\Sigma/(j\alpha_m)|\Phi_m(\theta_i)|^2$ represent the effective acoustic impedance of the two Helmholtz resonators, including the evanescent waves supported by the acoustic grating, and $\tilde{Z}_{12} = \sum_{m\neq 0,-1} R_\Sigma/(j\alpha_m)\cos m\pi|\Phi_m(\theta_i)|^2$ represents the coupling of the two Helmholtz resonators through the evanescent waves. Note that $\tilde{Z}_0$ and $\tilde{Z}_{-1}$ are real numbers, whereas $\tilde{Z}_a(1)$, $\tilde{Z}_a(2)$, and $\tilde{Z}_{12}$ are imaginary numbers. The real and imaginary parts of Eq. (5) are written as

$$\tilde{Z}_a(1)\tilde{Z}_a(2) + (\tilde{Z}_{-1} - \tilde{Z}_0)^2 - (\tilde{Z}_{12})^2 - (\tilde{Z}_{-1} + \tilde{Z}_0)^2 = 0, \tag{6a}$$

$$(\tilde{Z}_{-1} - \tilde{Z}_0)(\tilde{Z}_a(1) + \tilde{Z}_a(2)) + 2(\tilde{Z}_{-1} + \tilde{Z}_0)\tilde{Z}_{12} = 0. \tag{6b}$$

It is verified that the Bragg condition can also be obtained from Eq. (6b), because the two relations $\tilde{Z}_{-1} - \tilde{Z}_0 = 0$ and $\tilde{Z}_{12} = 0$ are simultaneously satisfied along the Bragg line, $k\sin\theta_i = \pi/\Lambda$. By substituting the Bragg condition into Eq. (6a), we obtain $\tilde{Z}_a(1)\tilde{Z}_a(2) > 0$, which means that perfect blazing occurs at a frequency lying between the two Helmholtz resonances owing to coupling.

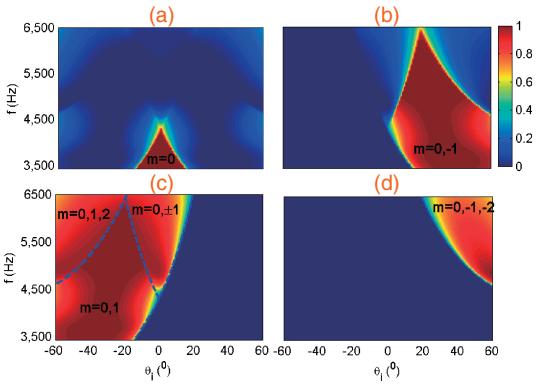

Fig. 2. Theoretical results for the dependence of the normalized reflected power R_m on the incident angle θ_i and frequency f for four diffraction orders, the 0th (a), −1st (b), 1st (c), and −2nd (d), where the parameters of the acoustic grating are given in Fig. 1. Note that regions with different propagating diffraction orders, determined by the relation $-1 \le \sin\theta_i + m\lambda/\Lambda \le 1$, can also be discerned. For example, "$m = 0, 1$" in (c) represents a region in which the 0th and 1st diffraction order are propagating. In addition, dashed lines in (c) mark the boundary of different regions.

For multiple coupled Helmholtz resonators per cell, coupling can induce perfect blazing not only at points along the Bragg line, but also at points in pairs on opposite sides of the Bragg line. These points are called the non-Bragg blazing points and should satisfy the relation $\sin\theta_1 + \sin\theta_2 = \lambda/\Lambda$,[5] where θ_1 and θ_2 are the two incident angles occurring in pairs. If a non-Bragg blazing point exists for an acoustic grating based on two coupled Helmholtz resonators per cell, the non-Bragg condition can be verified by Eq. (6).

A particle swarm optimization algorithm[15] is adopted to obtain the best parameters of acoustic gratings with the constraint of minimized specular reflection in a wide frequency range at a given incident angle. The designed acoustic grating in Fig. 1(b) is obtained by setting the incident angle $\theta_i = 30°$, which is determined by the Bragg condition for the central wavelength $\lambda = \Lambda$. Figure 2 shows the theoretical result for the normalized reflected power R_m for four diffraction orders, where the normalized reflected power for the propagating diffraction order is defined as $R_m = |r_m|^2\cos\theta_{mr}/\cos(\theta_i)$, with θ_{mr} being the reflected angle of the mth diffraction order. It is shown in Fig. 2(a) that the normalized specular reflected power R_0 is close to zero over a wide frequency-angle range, and most of the incident power is diffracted into the −1st (or 1st) order when the incident angle and frequency are located in the region with the propagating diffraction orders "$m = 0, -1$" in Fig. 2(b) [or "$m = 0, 1$" in Fig. 2(c)]. This means that acoustic negative reflection occurs not only at a positive incident angle in the region "$m = 0, -1$", but also at a negative incident angle in the region "$m = 0, 1$" over a broad frequency range.

To understand the phenomenon of broadband and wide-angle acoustic negative reflection by our designed acoustic grating, the normalized specular reflected power R_0 in Fig. 2(a) is depicted according to the dB level ($10\log_{10} R_0$) in Fig. 3(a). It is observed that five poles (Bragg blazing

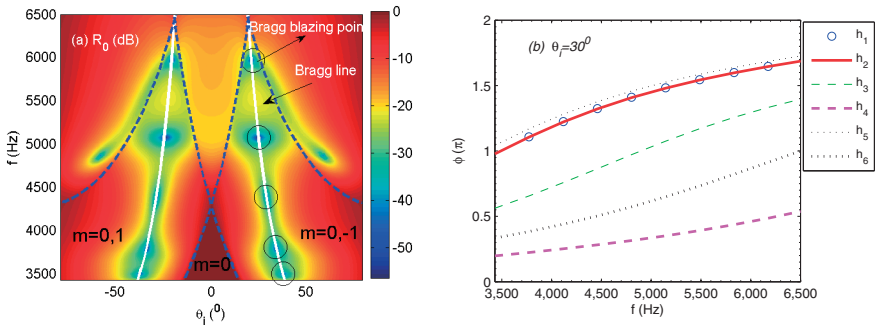

Fig. 3. (a) dB level of the normalized specular reflected power R_0, which is shown in Fig. 2(a). Dashed lines mark the boundaries of regions with different propagating diffraction orders; thick white lines represent the Bragg line determined by the Bragg condition, and the Bragg blazing points are marked by five circles with their centers located at (22°, 5968 Hz), (25°, 5076 Hz), (29°, 4390 Hz), (34°, 3807 Hz), and (38°, 3499 Hz). (b) Reflected phase of the acoustic grating having a single Helmholtz resonator per cell, where the lattice constant is reduced to $\Lambda/6$. Note that the six cavity heights are the same as those in Fig. 1.

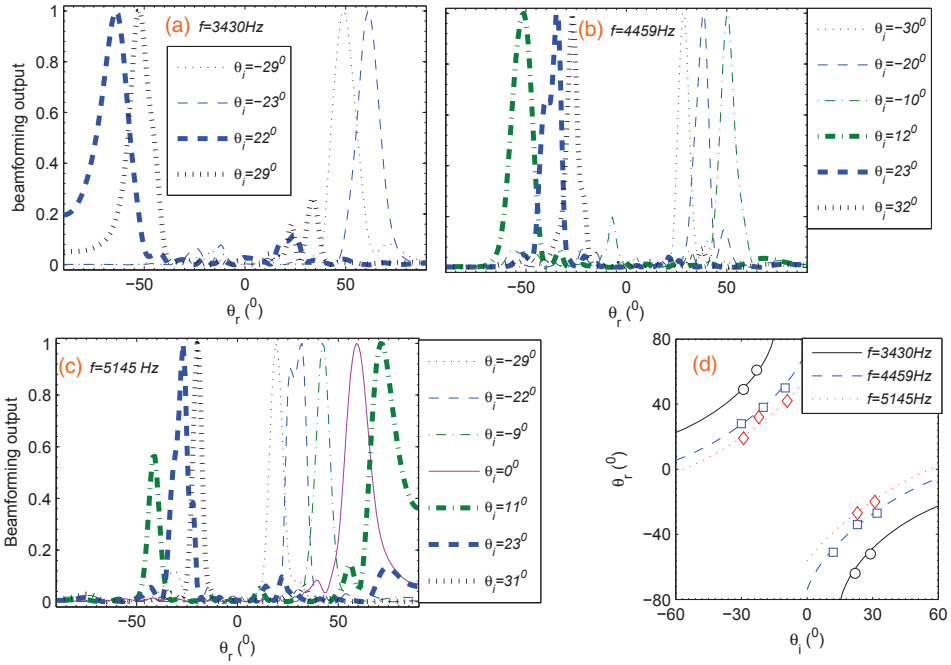

Fig. 4. Experimental results for the dependence of the beamforming output on the reflected angle for different incident angles at frequency $f = 3430$ Hz (a), $f = 4459$ Hz (b), and $f = 5145$ Hz in (c). (d) Dependence of the reflected angle on the incident angle, where the lines represent the theoretical result ($k \sin\theta_r = k \sin\theta_i \pm 2\pi/\Lambda$), and the symbols "○", "□", and "◇" represent the experimental results for the reflected angle at which the maximum beamforming output is achieved. Note that the incident angles in (a), (b), and (c) are determined by experiment.

points) are located in the region "$m = 0, -1$" (or in the region "$m = 0, 1$") along the Bragg line. These poles are related to the coupled resonances induced by the Helmholtz resonators and the couplings among them, which broaden the bandwidth and the range of incident angle at which minimized specular reflection is achieved, and thus lead to broadband and wide-angle acoustic negative reflection. It is seen from Fig. 3(b) that the reflected phase does not cover the entire 2π range over a broad frequency range, which means that wavefront manipulation by our designed acoustic grating differs from that based on the generalized Snell's law.[16–20] Note that when the difference in the phase modulation of the local reflection coefficient covers the entire 2π range for a metasurface period, wavefront manipulation by the generalized Snell's law is nearly perfect. However, because of the frequency dependence of the phase, the difference in the phase modulation cannot cover the entire 2π range over a broad frequency range, resulting in the appearance of multiple diffraction peaks, which cannot be described by the generalized Snell's law, but can be explained using the diffraction equation.[21]

In an experiment, a sample of 20 unit cells of height 3 cm is fabricated by three-dimensional (3D) printing. An array of 15 loudspeakers located at an approximate distance of 2 m from the acoustic grating is used to generate a localized approximately planar wavefront by inserting a different resistance in series with each loudspeaker. The intervals between the neighboring loudspeakers are 4.7 cm for the frequency 3430 Hz ($k\Lambda = 0.8 \times 2\pi$), 3.7 cm for 4459 Hz ($k\Lambda = 1.04 \times 2\pi$), and 3 cm for 5145 Hz ($k\Lambda = 1.2 \times 2\pi$). By rotating the loudspeaker array, six nominal incident angles, $\theta_i = \pm 10°$, $\pm 20°$, $\pm 30°$, are chosen according to the dimensions of the waveguide. To accurately obtain the incident and reflected angles in our experiment, a conventional beamforming method[22] is used to determine the incident angle from the measured sound pressure along the line marked in Fig. 1(a) without a sample and the reflected angle from the difference between the sound pressures obtained with and without a sample in the waveguide. Note that the sound pressure is obtained by a probe microphone placed behind the sample at a distance of 10.5 cm and moved along the measurement line in $\lambda/6$ steps by a stepping motor.

Figures 4(a)–4(c) show the beamforming output for different incident angles at three frequencies. In Fig. 4(d), acoustic negative reflection occurs at both positive and negative

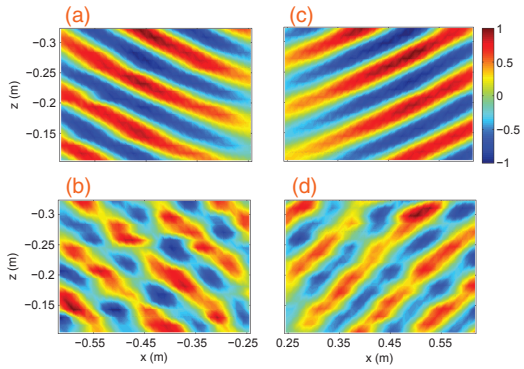

Fig. 5. Measurement of the distribution of the sound pressure over two separate measurement areas of the same size, $5\lambda \times 3\lambda$, marked in Fig. 1(a), for the frequency $f = 4459$ Hz. For the incident wave at $\theta_i = -20°$, we measure over an area on the left side of the waveguide (a) the sound pressure without a sample and (b) the reflected pressure, the reflected angle of which is $\theta_r = 36°$ as determined by a conventional beamforming method. For the incident wave at $\theta_i = 20°$, we measure over an area on the right side of the waveguide (c) the sound pressure without a sample and (d) the reflected pressure at angle $\theta_r = -40°$.

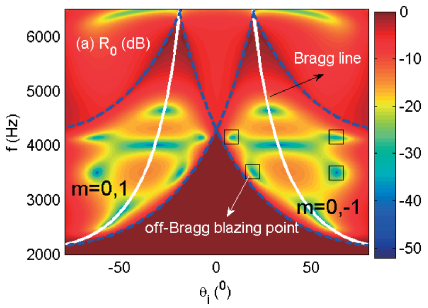

Fig. 6. dB level of the normalized specular reflected power R_0 for an acoustic grating from which the sixth Helmholtz resonator in the unit cell is removed, and the first five cavity heights are $h_1 = 0.0969\Lambda$, $h_2 = 0.1399\Lambda$, $h_3 = 0.3876\Lambda$, $h_4 = 0.3455\Lambda$, and $h_5 = 0.3397\Lambda$, respectively, and the other parameters of the acoustic grating are the same as those of that in Fig. 1. Dashed lines mark the boundaries of regions with different propagating diffraction orders. Thick white lines represent the Bragg line. In addition, four non-Bragg blazing points are marked by squares with their centers located at two pairs of positions: (8°, 4159 Hz) and (63°, 4159 Hz) for one pair, and (19°, 3516 Hz) and (63°, 3516 Hz) for the other.

incident angles in the regions with propagating diffraction orders "$m = 0, -1$" and "$m = 0, 1$"; Figs. 4(a)–4(c) show that most of the sound energy is reflected at the angle determined by $k \sin\theta_r = k \sin\theta_i \pm 2\pi/\Lambda$, where "$-$" indicates a positive incident angle, and "$+$" indicates a negative incident angle. Note that in Fig. 4(a), the results for the beamforming output at the incident angle $\theta_i = \pm 10°$ are not included because only the specular reflection is observed, which is consistent with the theoretical prediction. In addition, the experimental observation in Fig. 4(c) for incident angle $\theta_i = 11°$ deviates from the theoretical prediction. This result can be explained by the fact that this position (11°, 5145 Hz) is close to the region with the propagating diffraction order "$m = 0, \pm 1$", and imperfections in the sample lead to the disagreement. Figure 5 shows the distribution of the sound pressure at $f = 4459$ Hz, from which we know that acoustic negative reflection occurs at both positive and negative incident angles.

Note that only the Bragg blazing points in Fig. 3(a) are adopted to broaden the frequency and angle range of acoustic negative reflection, where the Bragg blazing points are located at incident angles not larger than 40°. However, non-Bragg blazing points can occur at large incident angles because they appear in pairs on opposite sides of the Bragg line. From the constraint of minimized specular reflection over a wide frequency range at incident angle $\theta_i = 60°$, we introduce the non-Bragg blazing points in Fig. 6. It is found that one cavity height can be made to approach zero by using the optimization algorithm; therefore, we design an acoustic grating from which the sixth Helmholtz resonator in the unit cell is removed. It is illustrated that the normalized reflected power R_0 is close to zero in a wide incident angle range owing to the combination of Bragg blazing points and non-Bragg blazing points, resulting in a broadband and wide-angle negative reflection in the region with propagating diffraction orders "$m = 0, -1$" (or "$m = 0, 1$").

In conclusion, a blazed acoustic grating based on multiple Helmholtz resonators per cell was developed. Theoretical and experimental results demonstrated a broadband and wide-angle negative reflection induced by interaction between the Helmholtz resonances and Bragg scatterings. The thickness of our designed acoustic grating, unlike that of a grating in which acoustic negative reflection is observed at a phononic crystal boundary,[11,12] is at the subwavelength scale. On the other hand, because the reflected phase need not cover the entire 2π range, and the response of the acoustic grating is nonlocal, wavefront manipulation by our designed acoustic grating also different from that described by the generalized Snell's law.

Acknowledgments We thank Huan Li and Meiling Hu for their assistance in carrying out the experiment. We wish to acknowledge the support of the National Science Foundation of China under Grant No. 11674293.

1) R. W. Wood, Philos. Mag. **4**, 396 (1902).
2) L. Rayleigh, Proc. R. Soc. London, Ser. A **79**, 399 (1907).
3) A. Hessel and A. A. Oliner, Appl. Opt. **4**, 1275 (1965).
4) A. Hessel, J. Schmoys, and D. Y. Tseng, J. Opt. Soc. Am. **65**, 380 (1975).
5) W. Chen, N. C. Beaulieu, D. G. Michelson, and E. V. Jull, IEEE Trans. Antennas Propag. **61**, 2342 (2013).
6) A. Wirgin and R. Deleuil, J. Opt. Soc. Am. **59**, 1348 (1969).
7) M. Memarian, X. Li, Y. Morimoto, and T. Itoh, Sci. Rep. **7**, 42286 (2017).
8) Z. Wei, H. Li, C. Wu, Y. Cao, J. Ren, Z. Hang, H. Chen, D. Zhang, and C. T. Chan, Opt. Express **18**, 12119 (2010).
9) Y. Zhang and X. Wang, Acta Acust. **36**, 191 (2011) [in Chinese].
10) G. Yu and X. Wang, J. Appl. Phys. **115**, 044913 (2014).
11) R. P. Moiseyenko, J. Liu, N. F. Declercq, and V. Laude, Appl. Phys. Lett. **102**, 034108 (2013).
12) D. Zhao, Y. Ye, S. Xu, X. Zhu, and L. Yi, Appl. Phys. Lett. **104**, 043503 (2014).
13) X. Yang, J. Yin, G. Yu, L. Peng, and N. Wang, Appl. Phys. Lett. **107**, 193505 (2015).
14) L. Qi, G. Yu, X. Wang, G. Wang, and N. Wang, J. Appl. Phys. **116**, 234506 (2014).
15) R. Poli, J. Kennedy, and T. Blackwell, Swarm Intell. **1**, 33 (2007).
16) N. Yu, P. Genevet, M. A. Kats, F. Aieta, J. Tetienne, F. Capasso, and Z. Gaburro, Science **334**, 333 (2011).
17) Y. Li, B. Liang, Z. Gu, X. Zou, and J. Cheng, Sci. Rep. **3**, 2546 (2013).
18) J. Zhao, B. Li, Z. Chen, and C. Qiu, Sci. Rep. **3**, 2537 (2013).
19) K. Tang, C. Qiu, M. Ke, J. Lu, Y. Ye, and Z. Liu, Sci. Rep. **4**, 6517 (2014).
20) Y. Xie, W. Wang, H. Chen, A. Konneker, B. Popa, and S. A. Cummer, Nat. Commun. **5**, 5553 (2014).
21) S. Larouche and D. R. Smith, Opt. Lett. **37**, 2391 (2012).
22) D. H. Johnson and D. E. Dudgeon, *Array Signal Processing: Concepts and Techniques* (Prentice-Hall, Englewood Cliffs, NJ, 1993).